

Transient wave imaging with limited-view data*

Habib Ammari[†] Mark Asch[‡] Lili Guadarrama Bustos[§]
Vincent Jugnon[¶] Hyeonbae Kang^{||}

Abstract

We consider for the wave equation the inverse problem of identifying locations of point sources and dipoles from limited-view data. Using as weights particular back-ground solutions constructed by the geometrical control method, we recover classical imaging algorithms by appropriately averaging limited-view data. We show both analytically and numerically that if one can construct accurately the geometric control, then one can perform imaging with the same resolution using limited-view as using full-view data.

Mathematics Subject Classification (MSC2000): 35R30, 35L05

Keywords: wave equation, reconstruction, limited-view data, geometric control, Kirchhoff algorithm, back-propagation, MUSIC

1 Introduction

In the recent works [6, 3, 5], we have investigated the imaging of small anomalies using transient full-view wave measurements. We have designed different approaches for locating them and reconstructing some information about their sizes and physical parameters. Our algorithms make use of complete view measurements. In the time-harmonic domain, Kirchhoff [27, 12, 8], back-propagation [2, 12], and multiple signal classification (MUSIC) [9, 10, 12, 24, 26, 35] algorithms, using one or multiple frequencies, have been investigated. The resolution of those algorithms is finite. It is essentially of the order one-half the wavelength.

In this work, we extend the algorithms developed for time-domain imaging with complete boundary measurements to the case with limited-view measurements. Our work is motivated by breast cancer photo-acoustic imaging, where free space assumption does not

*This work was partially supported by the ANR project EchoScan (AN-06-Blan-0089), the grant KRF-2008-220-C00002, the STAR project 190117RD, and KICOS project K20803000001-08B1200-00110.

[†]Department of Mathematics and Applications, Ecole Normale Supérieure, 45 Rue d'Ulm, 75005 Paris, France (habib.ammari@math.cnrs.fr).

[‡]Université de Picardie Jules Verne, Faculté de Maths-Info LAMFA, CNRS-UMR 6140, 33 rue Saint Leu 80039 Amiens Cedex 1, France (mark.asch@u-picardie.fr).

[§]Institut Langevin, ESPCI ParisTech, CNRS UMR 7587, 10 rue Vauquelin, 75231 Paris Cedex 05, France (Lili.Guadarrama@espci.fr).

[¶]Centre de Mathématiques Appliquées, CNRS UMR 7641, Ecole Polytechnique, 91128 Palaiseau, France (jugnon@cmap.polytechnique.fr).

^{||}Department of Mathematics, Inha University, Incheon 402-751, Korea (hbkang@inha.ac.kr).

hold. Moreover, measurements are only done on part of the boundary. For simplicity, we model here the small anomalies as point sources or dipoles. We refer the reader to [6, 3, 5] for rigorous derivations of these approximate models and their higher-order corrections. It is worth mentioning that in order to model a small anomaly as a point source or a dipole, one has to truncate the high-frequency component of the transient incident and reflected waves.

By using the geometrical control method [15], we show how to recover all the classical algorithms that have been used to image point sources and dipole locations. Our main finding in this paper is that if one can construct accurately the geometric control then one can perform imaging with the same resolution using partial data as using complete data. The reconstruction is via classical algorithms obtained by appropriately averaging the limited-view data. Even though this is natural, it has never been shown analytically nor numerically elsewhere. The idea of averaging was introduced in [1], where only a Fourier-type algorithm was developed. In this paper, we provide a systematic way to derive several other classical imaging algorithms using such an idea. Our algorithms here apply equally well to the case of many source points or dipole locations and are robust with respect to perturbations of the boundary. This is quite important in real experiments since one does not necessarily know the non-accessible part of the boundary with good accuracy.

The paper is organized as follows. In Section 2 we provide a key identity based on the averaging of the limited-view data, using weights constructed by the geometrical control method. Section 3 is devoted to developing, for different choices of weights, Kirchhoff-, back-propagation-, MUSIC-, and arrival time-type algorithms for transient imaging with limited-view data. In Section 4 we discuss potential applications of the method in emerging biomedical imaging. In Section 5 we present results of numerical experiments and comparisons among the proposed algorithms. It is worth mentioning in connection with this paper that the control method has been used successfully for solving other inverse problems and illustrating the deep connection between inverse problems and control theory; see for example [16]. We shall also refer to Bardos [14] for an interpretation of the time-reversal experiment by Fink and his group [28, 29] using control theory.

2 Geometric control

Let Ω be a bounded domain in \mathbb{R}^d , $d = 2$ or 3 . For simplicity, we assume that $\partial\Omega$ is smooth, although this condition could be considerably weakened. Let ν be the outward normal to $\partial\Omega$.

Throughout this paper, we shall use standard L^2 -based Sobolev spaces. The notation H^1 is used to denote those functions which, along with all their first-order derivatives, are in L^2 . H_0^1 denotes the closure of C_0^∞ in the norm of H^1 . We shall also need the space H^{-1} , which is defined as the dual (using an L^2 -inner product) of H_0^1 .

The basic model to be considered in this paper is the following wave equation:

$$\frac{\partial^2 p}{\partial t^2}(x, t) - c^2 \Delta p(x, t) = 0, \quad x \in \Omega, \quad t \in]0, T[, \quad (2.1)$$

for some final observation time T , with the Dirichlet boundary condition

$$p(x, t) = 0 \quad \text{on } \partial\Omega \times]0, T[, \quad (2.2)$$

the initial conditions

$$p(x, t)|_{t=0} = 0 \quad \text{in } \Omega, \quad (2.3)$$

and the point source initial data

$$\partial_t p(x, t)|_{t=0} = \delta(x - z) \quad \text{or} \quad \partial_t p(x, t)|_{t=0} = m_0 \cdot \nabla \delta(x - z) \quad \text{in } \Omega. \quad (2.4)$$

Here δ is the Dirac function at 0, c is the acoustic speed in Ω which we assume to be constant, and m_0 is a constant nonzero vector. We suppose that T is large enough so that

$$T > \frac{\text{diam}(\Omega)}{c}. \quad (2.5)$$

The purpose of this paper is to design efficient algorithms for reconstructing the location z from boundary measurements of $\frac{\partial p}{\partial \nu}$ on $\Gamma \times]0, T[$, where $\Gamma \subset \partial\Omega$.

Suppose that T and Γ are such that they geometrically control Ω , which roughly means that every geometrical optic ray, starting at any point $x \in \Omega$, at time $t = 0$, hits Γ before time T at a nondiffractive point; see [15, 34]. Let $\beta \in \mathcal{C}_0^\infty(\Omega)$ be a cutoff function such that $\beta(x) \equiv 1$ in a sub-domain Ω' of Ω , which contains the source point z .

For any function $w \in H^1(\Omega)$, we can construct by the Hilbert Uniqueness Method (HUM) of Lions [41] a unique $g_w(x, t) \in H_0^1(0, T; L^2(\Gamma))$ in such a way that the unique weak solution $v \in \mathcal{C}^0(0, T; L^2(\Omega)) \cap \mathcal{C}^1(0, T; H^{-1}(\Omega))$ of the wave equation

$$\frac{\partial^2 v}{\partial t^2} - c^2 \Delta v = 0 \quad \text{in } \Omega \times]0, T[, \quad (2.6)$$

$$v = 0 \quad \text{on } \partial\Omega \setminus \bar{\Gamma} \times]0, T[, \quad (2.7)$$

$$v = g_w \quad \text{on } \Gamma \times]0, T[, \quad (2.8)$$

$$v(x, 0) = c^2 \beta(x) w(x), \quad \partial_t v(x, 0) = 0 \quad \text{in } \Omega, \quad (2.9)$$

satisfies the final conditions

$$v|_{t=T} = \frac{\partial v}{\partial t}|_{t=T} = 0 \quad \text{in } \Omega. \quad (2.10)$$

The role of the cutoff function β is to have the initial condition $v|_{t=0}$ belong to $H_0^1(\Omega)$. Note that since the point sources we are looking for are supposed to be away from the boundary, β does not play any role in the imaging procedures below.

The HUM is constructive and allows to compute the control g_w . A detailed study of the algorithm can be found in [31], [32], [33], [13], and [49, 37]. A new implementation of the algorithm using conjugate gradient iteration on a bi-grid unstructured mesh is described in Section 5.1. Our implementation is based on a finite element method (in the space variable) and allows us to handle general geometries and meshes. It is also worth emphasizing that the HUM produces an ill-posed problem. If the initial datum w is highly oscillating, then the HUM can not produce a stable solution g_w .

Now, multiplying (2.1) by v and integrating over $\Omega \times [0, T]$ leads to the key identity of this paper:

$$\int_0^T \int_\Gamma \frac{\partial p}{\partial \nu}(x, t) g_w(x, t) d\sigma(x) dt = w(z) \quad \text{or} \quad -m_0 \cdot \nabla w(z). \quad (2.11)$$

Note that in the full-view case ($\Gamma = \partial\Omega$), no more boundary conditions are imposed on v and consequently, there are many families of explicit functions v satisfying (2.6) and (2.10).

For example, those used in [3] as probe functions correspond to one of the following choices for w in Ω :

$$w(x) := \frac{\delta\left(\tau - \frac{|x-y|}{c}\right)}{4\pi|x-y|} \quad \text{in three dimensions} \quad (2.12)$$

or

$$w(x) := \delta\left(\tau - \frac{1}{c}\theta \cdot x\right) \quad \text{in two dimensions,} \quad (2.13)$$

where θ is a unit vector and τ a scalar parameter. The functions defined in (2.12) and (2.13) are respectively families of spherical and plane waves.

3 Imaging algorithms

In this section, we only consider the initial condition $\partial_t p(x, t)|_{t=0} = \delta(x - z)$ in Ω . One can treat the case of the initial data $\partial_t p(x, t)|_{t=0} = m_0 \cdot \nabla \delta(x - z)$ in exactly the same way. Using the functions v constructed by the geometrical control method with different choices of initial data w , one recovers several classical algorithms for imaging point sources. For simplicity, we only consider a single point source, but the derived algorithms are efficient for locating multiple sources as well. The reader is referred to [23] for a review on source localization methods.

3.1 Kirchhoff algorithm

Let $y \in \mathbb{R}^d \setminus \overline{\Omega}$, $d = 2, 3$, and ω be a positive parameter. Set

$$w(x) = e^{i\omega|x-y|}, \quad x \in \Omega.$$

Then, for a given search point z^S in Ω , we have from (2.11)

$$\begin{aligned} \int_{\mathbb{R}} e^{-i\omega|z^S-y|} \int_0^T \int_{\Gamma} \frac{\partial p}{\partial \nu}(x, t) g_w(x, t) d\sigma(x) dt d\omega &= \int_{\mathbb{R}} e^{-i\omega(|z^S-y|-|z-y|)} d\omega \\ &= 2\pi\delta(|z^S-y|-|z-y|). \end{aligned} \quad (3.1)$$

At this point, it is worth mentioning that (3.1) cannot be achieved as it requires a wavenumber ω covering the whole real line. The difficulty lies in computing the function g_w in the control problem, specially for high frequencies. As will be shown later, this is what limits the resolution.

Taking now virtual points y outside Ω yields then a first algorithm for finding z . In fact, let $\omega_k, k = 1, \dots, K$, be a set of wavenumbers and let y_1, \dots, y_N , be a set of virtual points. To find the location z one maximizes over z^S the following imaging functional:

$$\mathcal{I}_{\text{KI}}(z^S) := \frac{1}{K} \Re e \sum_{\omega_k} \sum_{y_n} e^{-i\omega_k|z^S-y_n|} \int_0^T \int_{\Gamma} \frac{\partial p}{\partial \nu}(x, t) g_{w_{k,n}}(x, t) d\sigma(x) dt,$$

where $w_{k,n}(x) = e^{i\omega_k|x-y_n|}$. We say that this algorithm of Kirchhoff-type since \mathcal{I}_{KI} is a wavenumber integration of a superposition of phase-conjugated data, $w_{k,n}$.

If the set of wavenumbers $\omega_k \in [-\omega_{\max}, \omega_{\max}]$ is equi-distributed and K is large enough, then

$$\mathcal{I}_{\text{KI}}(z^S) \approx 2\pi \sum_{y_n} \frac{\sin \omega_{\max} |z^S - y_n| - |z - y_n|}{\omega_{\max} |z^S - y_n| - |z - y_n|}. \quad (3.2)$$

Define the resolution of the imaging functional \mathcal{I}_{KI} to be the full width of the point spread function, $2\pi \sum_{y_n} \frac{\sin \omega_{\max} |z^S - y_n| - |z - y_n|}{\omega_{\max} |z^S - y_n| - |z - y_n|}$, at its half maximum; see for example [2, page 35]. Then, if $|z^S - y_n| \gg 1$ and $|z - y_n| \gg 1$, then

$$\mathcal{I}_{\text{KI}}(z^S) \approx 2\pi \sum_{y_n} \frac{\sin \omega_{\max} |(z^S - z) \cdot y_n / |y_n||}{\omega_{\max} |(z^S - z) \cdot y_n / |y_n||},$$

and therefore, the resolution of \mathcal{I}_{KI} is of order one-half the wavelength, $2\pi/\omega_{\max}$. Moreover, in that case, $N = d$, the space dimension, is enough to locate z . But having a few more virtual control points y_n enhances the performance of the imaging functional \mathcal{I}_{KI} in the presence of measurement noise via a higher effective signal-to-noise ratio.

If $\{y_n\}$ are not far-away from z and z^S , then N should be at least larger than d . Furthermore, (3.2) shows that the functional \mathcal{I}_{KI} attains its maximum at the intersection of

$$\left\{ z^S \in \Omega : |z - y_n| - \frac{\pi}{\omega_{\max}} \leq |z^S - y_n| \leq |z - y_n| + \frac{\pi}{\omega_{\max}} \right\}.$$

3.2 Back-propagation algorithm

Set ω to be a positive parameter. If one takes w to be a plane wave:

$$w(x) = e^{i\omega\theta \cdot x}, \quad \theta \in S^{d-1},$$

where S^{d-1} is the unit sphere in \mathbb{R}^d , then one computes for a given search point $z^S \in \Omega$,

$$\int_{S^{d-1}} e^{-i\omega\theta \cdot z^S} \int_0^T \int_{\Gamma} \frac{\partial p}{\partial \nu}(x, t) g_w(x, t) d\sigma(x) dt d\sigma(\theta) = \int_{S^{d-1}} e^{i\omega\theta \cdot (z - z^S)} d\sigma(\theta).$$

But

$$\int_{S^{d-1}} e^{i\omega\theta \cdot (z - z^S)} d\sigma(\theta) = \begin{cases} j_0(\omega|z - z^S|) & \text{for } d = 3, \\ J_0(\omega|z - z^S|) & \text{for } d = 2, \end{cases}$$

where j_0 is the spherical Bessel function of order zero and J_0 is the Bessel function of the first kind and of order zero.

Let $\theta_1, \dots, \theta_N$ be equidistant points on the unit sphere S^{d-1} . One plots at each point z^S in the search domain the following imaging functional:

$$\mathcal{I}_{\text{BP}}(z^S) := \frac{1}{N} \Re e \sum_{\theta_n} e^{-i\omega\theta_n \cdot z^S} \int_0^T \int_{\Gamma} \frac{\partial p}{\partial \nu}(x, t) g_{w_n}(x, t) d\sigma(x) dt,$$

where $w_n(x) = e^{i\omega\theta_n \cdot x}$.

The resulting plot will have a large peak at z and a point spread function given by j_0 for $d = 3$ and J_0 for $d = 2$. The resolution, *i.e.*, the full width of the point spread function, is

then of order one-half the wavelength, $2\pi/\omega$. Note that the higher the wavenumber ω is, the better is the resolution. However, high wavenumber oscillations cause numerical instabilities in the computations of g_{w_n} by the HUM method. Therefore, there is a trade-off between resolution and stability.

This algorithm is a back-propagation algorithm since \mathcal{I}_{BP} is a direction integration of a superposition of phase-conjugated data, w_n ; see for example [2, 12].

We shall now compare \mathcal{I}_{BP} and \mathcal{I}_{KI} . We first note that the control functions corresponding to plane and spherical waves are, up to a phase term, approximately the same. We have

$$g_{e^{i\omega|x-y|}} \approx e^{i\omega|y|} g_{e^{-i\omega x \cdot \theta}},$$

where $\theta = y/|y|$, provided that $|y-x| \gg 1$ for $x \in \Omega$. Then recall that if the virtual control points y_n are far-away from z and z^S , then d control points are enough to locate z via \mathcal{I}_{KI} . Moreover, in that case, \mathcal{I}_{KI} is an integration over wavenumbers of a superposition of phase conjugated data. It turns out that the imaging functional \mathcal{I}_{BP} is an integration over directions $y_n/|y_n|$ of approximately the same data for a single wavenumber ω . Furthermore, the imaging functional \mathcal{I}_{BP} has essentially the same resolution as \mathcal{I}_{KI} if $\omega = \omega_{\text{max}}$.

3.3 MUSIC algorithm

Take

$$w(x) = e^{i\omega(\theta-\theta') \cdot x}, \quad \theta, \theta' \in S^{d-1}.$$

It follows from (2.11) that

$$\int_0^T \int_{\Gamma} \frac{\partial p}{\partial \nu}(x, t) g_w(x, t) d\sigma(x) dt = e^{i\omega(\theta-\theta') \cdot z}.$$

In order to design a MUSIC algorithm for locating z , let $\theta_1, \dots, \theta_N$ be N unit vectors in \mathbb{R}^d . Define the matrix $A = (A_{nn'})_{n, n'=1}^N$ by

$$A_{nn'} := \int_0^T \int_{\Gamma} \frac{\partial p}{\partial \nu}(x, t) g_{w_{n, n'}}(x, t) d\sigma(x) dt,$$

with

$$w_{n, n'}(x) = e^{i\omega(\theta_n - \theta_{n'}) \cdot x}.$$

Let P be the orthogonal projection onto the range of A . Given any point z^S in the search domain, form the vector

$$h(z^S) := (e^{i\omega\theta_1 \cdot z^S}, \dots, e^{i\omega\theta_N \cdot z^S})^*,$$

where $*$ denotes the transpose. Then plot the MUSIC imaging functional:

$$\mathcal{I}_{\text{MU}}(z^S) := \frac{1}{\|(I - P)h(z^S)\|}.$$

Since

$$A = h(z)\bar{h}^*(z),$$

which shows that the range of A is spanned by $h(z)$, the resulting plot will have a large peak at z . Again, the higher the wavenumber ω is, the better is the resolution; see [2, page 163]. Moreover, as shown in [7], \mathcal{I}_{BP} has better stability property with respect to medium noise than \mathcal{I}_{MU} .

3.4 Arrival time and time-delay of arrival algorithms

Since c is supposed to be a known constant, arrival time and time-delay of arrival algorithms for locating z can be designed. Taking w to be a distance function,

$$w(x) = |y - x|,$$

to a virtual point y outside Ω yields arrival-time and time-delay of arrival algorithms. In fact, we have

$$\int_0^T \int_{\Gamma} \frac{\partial p}{\partial \nu}(x, t) g_w(x, t) d\sigma(x) dt = |y - z|. \quad (3.3)$$

Let y_1, \dots, y_N be N points (virtual receivers) and compute

$$r_n := \int_0^T \int_{\Gamma} \frac{\partial p}{\partial \nu}(x, t) g_{w_n}(x, t) d\sigma(x) dt, \quad (3.4)$$

with $w_n(x) = |y_n - x|$. Then, the point z can be found as the intersection of spheres of centers y_n and radii r_n .

We can use time-of-arrival differences instead of arrival times. This improves the robustness of the algorithm with respect to measurement noise; see for example [39]. Introduce the time-of-arrival difference, $t_{n,n'}$, between y_n and $y_{n'}$ as follows:

$$t_{n,n'} := \int_0^T \int_{\Gamma} \frac{\partial p}{\partial \nu}(x, t) (g_{w_n} - g_{w_{n'}})(x, t) d\sigma(x) dt.$$

In two-dimensions, at least $N = 2$ are required to locate z . The location z can be found as the intersection of two circles centered at two points outside the search region. In the three dimensional case, at least $N = 4$ sources are required to locate z as the intersection of three sets of hyperboloids by using time-of-arrival differences. See, for instance, [21, 47, 46, 22, 36, 17, 23].

In view of (3.1) and (3.3), arrival time and Kirchhoff algorithms have comparable performances for detecting a single point-like source. However, arrival time algorithm is not well-suited for identifying several point-like sources. Note also that the arrival time algorithm does not work if the point source initial condition is $a\delta(x - z)$ with unknown constant a while the Kirchhoff algorithm does not need to have an *a priori* knowledge of a .

Remark 3.1 *As we said in Section 2, in the full-view case there are no more boundary conditions to impose on v . However, it is still possible to apply the HUM to compute g_w and derive the analog of the imaging functionals \mathcal{I}_{KI} , \mathcal{I}_{BP} , and \mathcal{I}_{MU} . It is clear that they have the same resolution as those in the limited-view case.*

4 Applications to emerging biomedical imaging

In this section we show how to apply the designed algorithms to emerging biomedical imaging. Of particular interest are radiation force imaging, magneto-acoustic current imaging, and photo-acoustic imaging. In [25], the use of a reverberant cavity is proposed. Iterative regularization procedures to "generate" the absent data have been developed in [43, 42, 4]. A direct approach with pre-computation of a numerical filter has been provided in [40].

All of these papers dealt with imaging in free space. In that case, it is possible to apply Tikhonov regularization. However, in bounded domains, because of the multiple reflection from the boundary, regularization techniques do not apply. Our algorithms in this section seem to be the most natural and appropriate algorithms for imaging small anomalies inside a bounded domain from limited-view measurements in the time-domain. They can be viewed as a numerical filtering of the data in the case of a bounded domain.

4.1 Radiation force imaging

In radiation force imaging, one generates vibrations inside the organ, and acquires a spatio-temporal sequence of the propagation of the induced transient wave to estimate the location and the viscoelastic parameters of a small anomaly inside the medium. See, for instance, [18, 19, 6].

Let $d = 3$. Let z be the location of the anomaly. Let Ω be a large ball englobing the anomaly. In the far-field, the problem, roughly speaking, reduces to finding the location of the anomaly from measurements of the pressure p on $\partial\Omega \times]0, T[$, that is, the solution to

$$\frac{\partial^2 p}{\partial t^2}(x, t) - c^2 \Delta p(x, t) = 0, \quad x \in \mathbb{R}^3, \quad t \in]0, T[, \quad (4.1)$$

with the initial conditions

$$p(x, t)|_{t=0} = 0 \quad \text{and} \quad \partial_t p(x, t)|_{t=0} = m_0 \cdot \nabla \delta(x - z) \quad \text{in } \mathbb{R}^3. \quad (4.2)$$

See [6]. A time-reversal technique can be designed to locate the anomaly. Suppose that one is able to measure p and its normal derivative at any point x on $\partial\Omega$. If both p and its normal derivative on $\partial\Omega$ are time-reversed and emitted from $\partial\Omega$, then the time-reversed wave travels back to the location z of the anomaly. See again [6].

Suppose now that the measurements of p and its normal derivative are only done on the part Γ of $\partial\Omega$. Note first that

$$\frac{\partial p}{\partial \nu}|_{\partial\Omega \times]0, T[} = \Lambda_{\text{DtN}}[p|_{\partial\Omega \times]0, T[}],$$

where Λ_{DtN} is the Dirichlet-to-Neumann operator for the wave equation in $\mathbb{R}^3 \setminus \Omega$. For any function v satisfying (2.6), (2.9), and (2.10), integrating by parts yields

$$\int_0^T \int_{\partial\Omega} p(x, t) (\Lambda_{\text{DtN}}^*[v] + \frac{\partial v}{\partial \nu})(x, t) d\sigma(x) dt = m_0 \cdot \nabla w(z),$$

where Λ_{DtN}^* denotes the adjoint of Λ_{DtN} . Next, constructing by the geometrical control method, g_w such that v satisfies (2.6), (2.9), and (2.10), together with the boundary condition

$$\Lambda_{\text{DtN}}^*[v] + \frac{\partial v}{\partial \nu} = \begin{cases} 0 & \text{on } \partial\Omega \setminus \bar{\Gamma} \times]0, T[\\ g_w & \text{on } \Gamma \times]0, T[, \end{cases}$$

one obtains

$$\int_0^T \int_{\Gamma} p(x, t) g_w(x, t) d\sigma(x) dt = m_0 \cdot \nabla w(z).$$

Making similar choices for w to those in the previous section provide different algorithms for locating the anomaly.

4.2 Magneto-acoustic current imaging

In magneto-acoustic current imaging, one detects a pressure signal created in the presence of a magnetic field by electrically active tissues [38, 44, 45]. In the presence of an externally applied magnetic field, biological action currents, arising from active nerve or muscle fibers, experience a Lorentz force. The resulting pressure or tissue displacement contains information about the action current distribution.

Let $z \in \Omega$ be the location of an electric dipole, which represents an active nerve or muscle fiber, with strength c . The wave equation governing the induced pressure distribution p is (2.1), with the boundary condition (2.2), the initial conditions (2.3), and

$$\partial_t p(x, t)|_{t=0} = \delta(x - z) \quad \text{in } \Omega. \quad (4.3)$$

The algorithms constructed in the previous section apply immediately to finding z from partial boundary measurements of the normal derivative of p .

4.3 Photo-acoustic imaging

The photo-acoustic effect refers to the generation of acoustic waves by the absorption of optical energy [48, 30]. In photo-acoustic imaging, energy absorption causes thermo-elastic expansion of the tissue, which in turn leads to propagation of a pressure wave. This signal is measured by transducers distributed on the boundary of the organ, which is in turn used for imaging optical properties of the organ. Mathematically, the pressure p satisfies (2.1) with the boundary condition (2.2) and the initial conditions

$$p(x, t)|_{t=0} = a\delta(x - z) \quad \text{in } \Omega, \quad (4.4)$$

and

$$\partial_t p(x, t)|_{t=0} = 0 \quad \text{in } \Omega. \quad (4.5)$$

Here a is the absorbed energy.

Construct by the geometrical control method a function $v(x, t)$ satisfying (2.6), the initial condition (2.9), the boundary condition $v = 0$ on $\partial\Omega \setminus \bar{\Gamma}$, and the final conditions (2.10). Choosing w as in Section 3 yields different detection algorithms.

5 Numerical illustrations

To test the geometrical control imaging approach, we implemented numerical simulations of both the forward problem, the wave equation (2.1)-(2.4), and the inverse problem where we compute the geometrical control function (2.6)-(2.8) and implement the inversion algorithms of Section 3.

To simulate the wave equation, we use a standard P1-finite element discretization in space and a finite difference scheme in time. For time-cost considerations, we settle with an explicit (leap-frog) scheme along with the use of mass lumping (row-sum technique).

The method we present here has been implemented and tested on various types of two-dimensional meshes. We will present results obtained on three different sets of meshes (see Figure 1 and Table 1):

- squareReg0 and squareReg2 are regular meshes of the unit square $[-0.5, 0.5]^2$. The meshes in squareReg2 are refinements of those in squareReg0.

- circle are unstructured meshes of the unit disc.

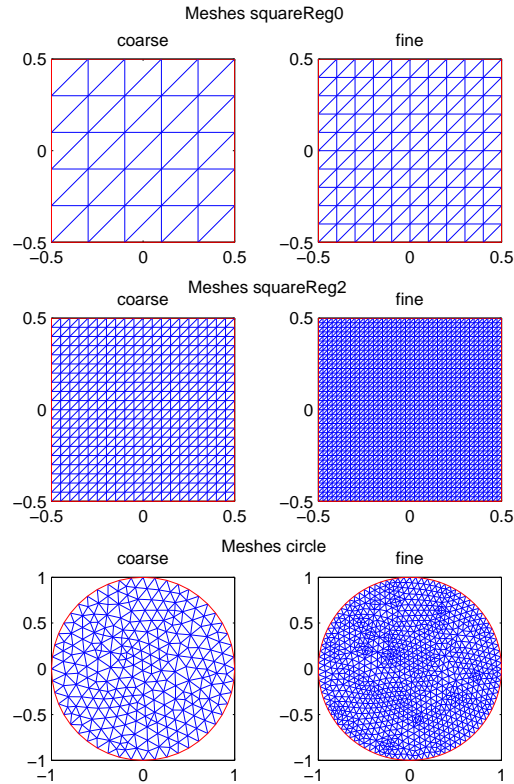


Figure 1: The coarse and fine meshes used on the square and circular geometries.

For computation of imaging functionals of Kirchhoff-, back-propagation-, and MUSIC-types, one has to be very careful with the wavenumber ω . One has to make sure that the function $w(x; \omega)$ is accurately represented on the meshes we use. This imposes strict limitations on the range of wavenumbers that can be used. It is worth mentioning that in practice the nature of experiments determines the range of wavenumbers and hence the opposite should be done, namely, the mesh should be adjusted to resolve those wavenumbers.

Finally, the considered initial conditions for the simulated measurements are $p(x, 0) = 0$ and $\frac{\partial p}{\partial t}(x, 0) = \delta_h(x_0)$, where δ_h is a Gaussian approximation of the Dirac distribution and $x_0 = [0.21 \ -0.17]$ (see Figure 2).

To illustrate the performance of our approach with regards to limiting the view, we apply the algorithm to both a full and a partial view setting. In both cases, the HUM is used to compute the function g_w defined by (2.8). For the square domain, we assume

| Set name | Coarse mesh | | | Fine mesh | | |
|------------|-------------|---------------|--------|------------|---------------|--------|
| | # of nodes | # of elements | $2h$ | # of nodes | # of elements | h |
| squareReg0 | 36 | 50 | 0.2 | 121 | 200 | 0.1 |
| squareReg2 | 441 | 800 | 0.05 | 1681 | 3200 | 0.025 |
| disc | 270 | 490 | 0.0672 | 1029 | 1960 | 0.0336 |

Table 1: Geometries and meshes.

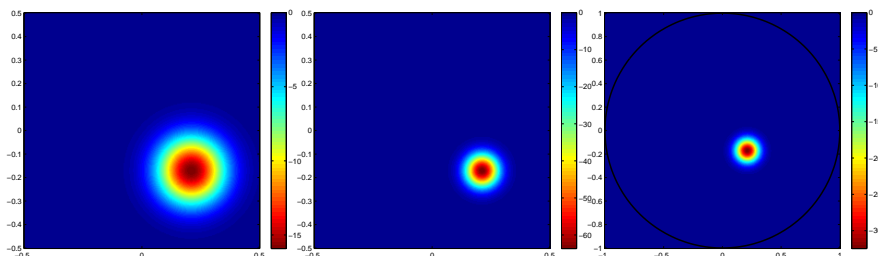


Figure 2: Gaussian approximations of a Dirac distribution, for the three geometries, used for the simulated measures.

measurements are taken only on two adjacent edges - this corresponds to the theoretical (and practical) limit that still ensures geometric controllability. For the circular domain, we assume measurements between angles $\frac{\pi}{4}$ and $\frac{3\pi}{2}$, as shown in Figure 3.

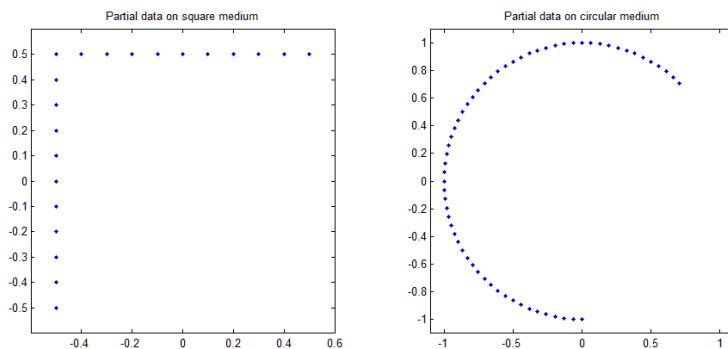


Figure 3: Limited-view observation boundaries for square and disc.

Before presenting the numerical results, we describe the numerical method used for computing the geometrical control, which is based on the HUM.

5.1 Geometrical control: HUM using conjugate gradient iteration on a bi-grid mesh

The control g_w such that the solution v to (2.6)-(2.9) satisfies the final conditions (2.10) has been shown to be unique provided that T and the control boundary Γ geometrically control Ω [15]. A systematic and constructive method for computing such a control is given by the HUM [41]. The method applies a conjugate gradient algorithm as follows:

- Let $e_0, e_1 \in H_0^1(\Omega) \times L^2(\Omega)$;
- Solve forwards on $]0, T[$ the wave equation

$$\begin{cases} \frac{\partial^2 \phi}{\partial t^2}(x, t) - c^2 \Delta \phi(x, t) = 0 & \text{in } \Omega \times]0, T[, \\ \phi(x, t) = 0 & \text{on } \partial\Omega \times]0, T[, \\ \phi(x, 0) = e_0(x), \quad \frac{\partial \phi}{\partial t}(x, 0) = e_1(x); \end{cases} \quad (5.1)$$

- Compute $\frac{\partial \phi}{\partial \nu}(x, t)$ on $\Gamma \times]0, T[$ and solve backwards the wave equation

$$\begin{cases} \frac{\partial^2 \psi}{\partial t^2}(x, t) - c^2 \Delta \psi(x, t) = 0 & \text{in } \Omega \times]0, T[, \\ \psi(x, t) = \begin{cases} 0 & \text{on } \partial\Omega \setminus \bar{\Gamma} \times]0, T[, \\ \frac{\partial \phi}{\partial \nu}(x, t) & \text{on } \Gamma \times]0, T[, \end{cases} \\ \psi(x, T) = 0, \quad \frac{\partial \psi}{\partial t}(x, T) = 0; \end{cases} \quad (5.2)$$

- Set

$$\Lambda(e_0, e_1) = \left(\frac{\partial \psi}{\partial t}(x, 0), -\psi(x, 0) \right); \quad (5.3)$$

- The solution v of (2.6)-(2.9) can be identified with ψ when

$$\Lambda(e_0, e_1) = (0, -c^2 \beta(x)w(x))$$

and $g_w(x, t) = \psi(x, t)$ on $\Gamma \times]0, T[$.

Remark 5.1 *In the case where the initial condition is a pressure field (e.g., photo-acoustics) $p(x, 0) = p_0(x)$, $\frac{\partial p}{\partial t}(x, 0) = 0$, we need to have $v(x, 0) = 0$, $\frac{\partial v}{\partial t}(x, 0) = c^2 \beta(x)w(x)$. This can be easily obtained by solving: $\Lambda(e_0, e_1) = (c^2 \beta(x)w(x), 0)$.*

To proceed, we use a conjugate gradient algorithm on a discretized version Λ_h of the operator defined in (5.3), where we solve the wave equation using the finite-element (in space) finite-difference (in time) discretization described previously. To deal with unwanted effects linked with high spatial oscillations, we use a bi-grid method of Glowinski [31] based on a fine mesh with discretization length h and a coarse mesh with length $2h$. The wave equation is solved on the fine mesh and the residuals of Λ_h are computed after projection onto the coarse mesh. The implementation follows the lines of the one proposed in [13].

However, in this paper, the HUM is for the first time implemented for general geometries and unstructured meshes.

Let us define I_h^{2h} and I_{2h}^h to be the projectors from the fine mesh to the coarse mesh and vice versa. Let Δt be the time-step and let \mathcal{T}_h be a finite-element triangulation of Ω . Suppose we want to control the pair of initial conditions (u_0, u_1) , that is, we want to solve

$$\Lambda(e_0, e_1) = (u_1, -u_0).$$

The conjugate gradient algorithm is now as follows:

- Let e_0^0, e_1^0 be given initial guesses on the coarse mesh;
- Solve numerically (5.1) forwards with initial conditions $I_{2h}^h[e_0^0], I_{2h}^h[e_1^0]$ to get ϕ^0 on the fine mesh. Use ϕ^0 to solve backwards (5.2). Get ψ^0 on the fine grid and arrive at

$$\Lambda_h(e_0^0, e_1^0) = \left(\frac{\psi^0(\Delta t) - \psi^0(-\Delta t)}{2\Delta t}, -\psi^0(0) \right);$$

- Compute the initial residuals $g^0 = \{g_0^0, g_1^0\}$ on the coarse grid, where g_0^0 is the solution to the following boundary-value problem:

$$\begin{cases} -\Delta g_0^0 = I_h^{2h} \left[\frac{\psi^0(\Delta t) - \psi^0(-\Delta t)}{2\Delta t} \right] - I_h^{2h}[u_1] & \text{in } \Omega, \\ g_0^0 = 0 & \text{on } \partial\Omega, \end{cases}$$

and

$$g_1^0 = \psi^0(0) - I_h^{2h}[u_0];$$

- If the norm of the residuals

$$\|\{g_0^0, g_1^0\}\|_h^2 := \int_{\mathcal{T}_h} |g_1^0|^2 + |\nabla g_0^0|^2$$

is small enough, we have our solution, else we set the first search direction $w^0 = g^0$ and start the conjugate gradient;

- Suppose we know $e^k = \{e_0^k, e_1^k\}$, $g^k = \{g_0^k, g_1^k\}$ and $w^k = \{w_0^k, w_1^k\}$;
- Solve numerically (5.1) forwards with initial conditions $I_{2h}^h[w_0^k], I_{2h}^h[w_1^k]$ and solve (5.2) backwards both on the fine grid to get ψ^k ;
- Compute the remaining residuals $\xi^k = \{\xi_0^k, \xi_1^k\}$ on the coarse grid, where ξ_0^k is the solution to the following boundary-value problem:

$$\begin{cases} -\Delta \xi_0^k = I_h^{2h} \left[\frac{\psi^k(\Delta t) - \psi^k(-\Delta t)}{2\Delta t} \right] & \text{in } \Omega, \\ \xi_0^k = 0 & \text{on } \partial\Omega, \end{cases}$$

and

$$\xi_1^k = \psi^k(0);$$

- Calculate the length of the step in the w^k direction

$$\rho^k = \frac{\|g^k\|_h}{\langle \xi^k, w^k \rangle_h},$$

where $\langle \xi^k, w^k \rangle_h = \int_{\mathcal{T}_h} \nabla \xi_0^k \cdot \nabla w_0^k + \xi_1^k w_1^k$;

- Update the quantities

$$\begin{aligned} e^{k+1} &= e^k - \rho^k w^k, \\ g^{k+1} &= g^k - \rho^k \xi^k; \end{aligned}$$

- If $\|g^{k+1}\|_h$ is small, then e^{k+1} is our solution, else compute

$$\gamma^k = \frac{\|g^{k+1}\|_h}{\|g^k\|_h},$$

and set the new descent direction

$$w^{k+1} = g^{k+1} + \gamma^k w^k.$$

Remark 5.2 (Remarks on the numerical procedure) *We first note that, compared to [32], [33] and [13], the novelty of our numerical procedure is that it uses a finite element method on a general mesh with a bi-grid regularization. On the other hand, in the case of finite difference method on the unit square, the numerical procedure described in this section has been proved to converge [37]. This result can be easily extended in the case of a finite element method on a regular mesh. However, convergence results for more general meshes are not available yet. They will be the subject of a future study.*

5.2 Reconstruction results

We present here some results obtained by algorithms presented in Section 3. For each algorithm we consider both the full view and the partial view cases. The computed point spread functions are exactly the same in both cases. We search over a $2^8 \times 2^8$ grid covering the domain.

- **Kirchhoff algorithm.** We limit ourselves to the wavenumber range: $W = [-\omega_{\max}, \omega_{\max}]$ with a step-size $\Delta\omega = \omega_{\max}/n_\omega$ where ω_{\max} and n_ω depend on the mesh coarseness. To be more precise, we require a minimum of 10 points per wavelength on the fine mesh, which yields the heuristic rule

$$\omega_{\max} = \frac{2\pi}{10hL},$$

where h is the characteristic size of the mesh and L is the size of the domain. This gives $\omega_{\max} = 6$ for squareReg0, $\omega_{\max} = 25$ for squareReg2 and $\omega_{\max} = 12$ for disk. For time considerations we choose a reduced array of three virtual sources

- $Y = \{[0.6 \ -0.6], [0.6 \ 0], [0.6 \ 0.6]\}$ for the square domain.
- $Y = \{[1 \ -1], [1 \ 0], [1 \ 1]\}$ for the circular domain.

We compute and represent the function $\mathcal{I}_{\text{KI}}(z^S)$ for z^S on the fine mesh. The estimated position is at the maximum of $\mathcal{I}_{\text{KI}}(z^S)$. Reconstruction results are given in Figure 4.

- **Back-propagation algorithm.** We choose ω_{max} (the highest wavenumber used in the Kirchhoff algorithm) as a working wavenumber and a 50-point discretization of the unit circle for θ .

We compute and represent the function $\mathcal{I}_{\text{BP}}(z^S)$ for z^S on the fine mesh. The estimated position is at the maximum of $\mathcal{I}_{\text{BP}}(z^S)$. Results are given in Figure 5.

- **Arrival-time algorithm.** We consider two virtual receivers $Y = \{[0 \ 0.6]; [0.6 \ 0]\}$ for the square domain. For each receiver we compute the value of $r_k = |x_0 - y_k|$, where x_0 is the position of the source and y_k the position of the virtual receiver. We represent the circles $\mathcal{C}(y_k, r_k)$ and their intersections. Results are given in Figure 6.
- **MUSIC algorithm.** Working with the same values of ω and N as for the back-propagation algorithm, we compute and represent the function $\mathcal{I}_{\text{MU}}(z^S)$ for z^S on the fine mesh. The estimated position is at the maximum of $\mathcal{I}_{\text{MU}}(z^S)$. Reconstruction results are given in Figure 7.

In Table 2 we give the estimations x_{est} of the source location $x_0 = [0.21 \ -0.17]$ for each algorithm, and the error $|x_0 - x_{\text{est}}|$.

5.3 Case of multiple sources

Except for the arrival-time algorithm, all the methods presented in this paper are well-suited for identifying several point-like sources. To illustrate this, we simulate measurements on squareReg2 with three sources located at $[-0.25 \ -0.25]$, $[0.25 \ -0.25]$ and $[0 \ 0.25]$.

- We apply the Kirchhoff imaging algorithm with a different set of virtual sources:

$$Y = \left\{ \left[\cos\left(\frac{2\pi j}{10}\right) \sin\left(\frac{2\pi j}{10}\right) \right], j = 1, \dots, 10 \right\}.$$

Since Kirchhoff peaks at the points at the intersection of the circles centered at the virtual receivers and passing through the sources, too few receivers can generate false positives, *i.e.*, points wrongly considered to be source locations. We thus take more virtual points than in the case of a single anomaly. Results are given in Figure 10.

- We run the back-propagation and MUSIC algorithms with exactly the same values of ω and N as before. Results are given in Figures 11 and 12 respectively.

5.4 Boundary perturbation

In real experiments, one does not necessarily know the uncontrolled part of the boundary with good accuracy. A major concern for real applications of the methods proposed in this paper is thus its robustness with respect to perturbations of the boundary.

| Algorithm | Mesh | View | x_{est} | $ x_0 - x_{est} $ |
|------------------|------------|---------|------------------|-------------------|
| Kirchhoff | squareReg0 | Full | [0.2019 -0.1823] | 0.0147 |
| | | Partial | [0.2098 -0.1902] | 0.0201 |
| | squareReg2 | Full | [0.2059 -0.1745] | 0.0062 |
| | | Partial | [0.2059 -0.1745] | 0.0062 |
| | disk | Full | [0.2000 -0.1764] | 0.0119 |
| | | Partial | [0.2000 -0.1764] | 0.0119 |
| Back-propagation | squareReg0 | Full | [0.2019 -0.1784] | 0.0117 |
| | | Partial | [0.1980 -0.1706] | 0.0120 |
| | squareReg2 | Full | [0.2098 -0.1745] | 0.0045 |
| | | Partial | [0.2098 -0.1745] | 0.0045 |
| | disk | Full | [0.2078 -0.1765] | 0.0068 |
| | | Partial | [0.2078 -0.1765] | 0.0068 |
| Arrival time | squareReg0 | Full | [0.1877 -0.1433] | 0.0348 |
| | | Partial | [0.1882 -0.1314] | 0.0444 |
| | squareReg2 | Full | [0.2050 -0.1768] | 0.0085 |
| | | Partial | [0.2048 -0.1774] | 0.009 |
| | disk | Full | [0.1802 -0.2196] | 0.0579 |
| | | Partial | [0.1790 -0.2119] | 0.0522 |
| MUSIC | squareReg0 | Full | [0.2098 -0.1784] | 0.0084 |
| | | Partial | [0.2020 -0.1745] | 0.0092 |
| | squareReg2 | Full | [0.2098 -0.1745] | 0.0045 |
| | | Partial | [0.2098 -0.1745] | 0.0045 |
| | disk | Full | [0.2078 -0.1765] | 0.0068 |
| | | Partial | [0.2078 -0.1765] | 0.0068 |

Table 2: Numerical results for localization of the source at $x_0 = [0.21 \ -0.17]$ using four algorithms and three geometries.

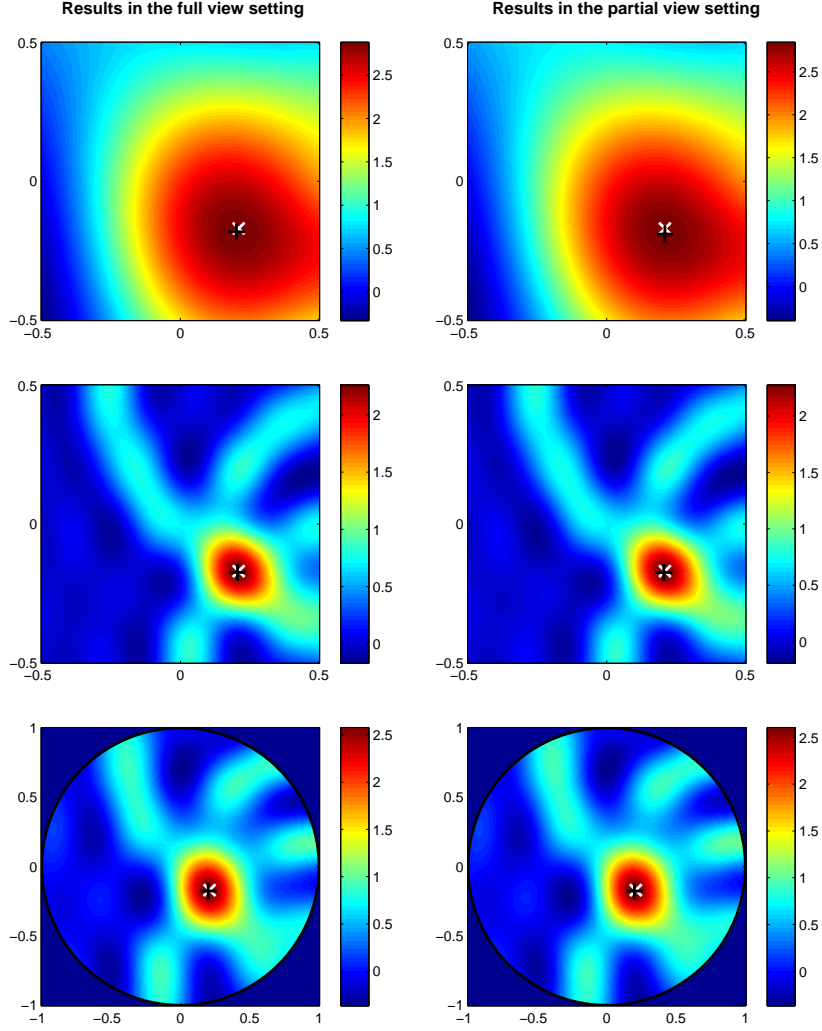


Figure 4: Kirchhoff results for the geometries of Table 1 - from top to bottom: squareReg0, squareReg2, disc. The (black/white) x denotes the (numerical/theoretical) center of the source.

We test our algorithms by perturbing the boundary nodes outwards

$$x_{i,\text{perturbed}} = x_i + \epsilon U n_{x_i},$$

where ϵ is the magnitude of perturbation, U is a uniform random variable in $[0, 1]$ and n_{x_i} is the outward normal at the point x_i . We simulate measurements on the perturbed mesh, which is then supposed unknown since we compute the geometric control on the unperturbed mesh.

To illustrate the results, we use squareReg2 with three levels of perturbation, $\epsilon = 0.01$,

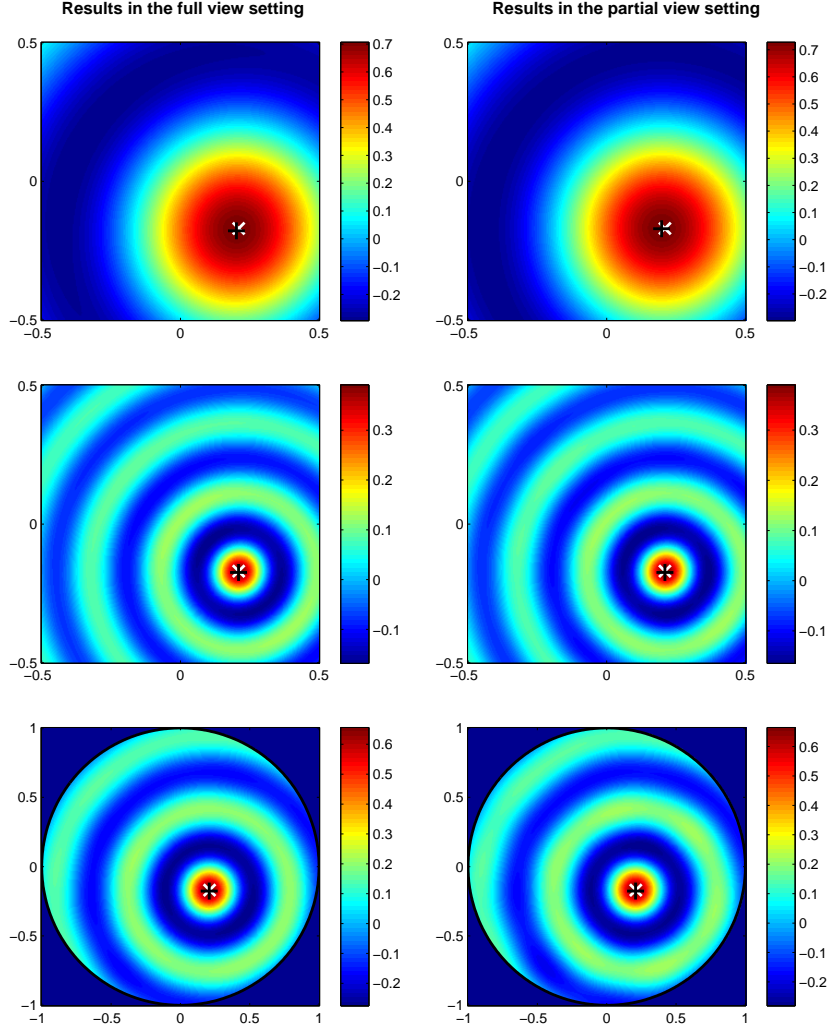


Figure 5: Back-propagation results for the geometries of Table 1 - from top to bottom: squareReg0, squareReg2, disc. The (black/white) x denotes the (numerical/theoretical) center of the source.

0.025 and 0.05 (see Figure 9) when there is a single source located at $[0.21 \ -0.17]$ as in Section 5.2.

We give the results, with the three perturbations, for the Kirchhoff (Figure 13), the back-propagation (Figure 14) and the arrival-time (Figure 15) algorithms. Modifying the mesh as we do generates smaller elements and thus changes the CFL condition for the wave-equation solver. Computation time becomes too expensive for the MUSIC algorithm. For this reason we do not present MUSIC results here.

As expected the estimation of the source position deteriorates as we increase the bound-

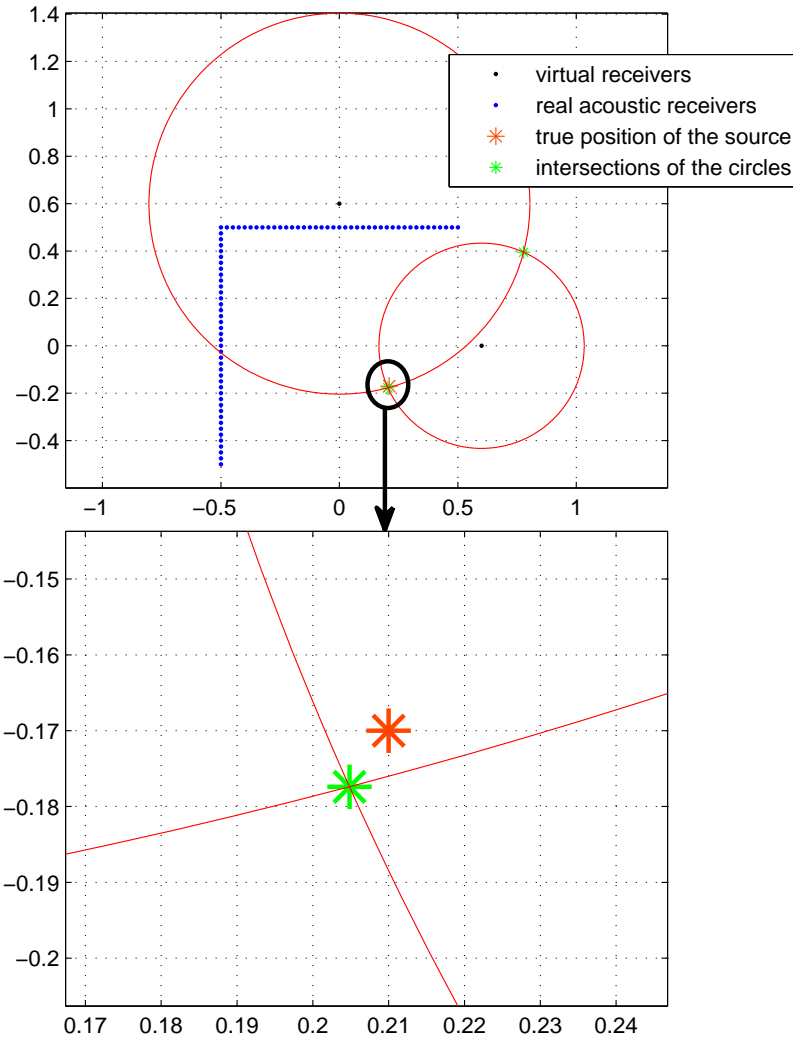


Figure 6: Example of arrival time results for squareReg2 geometry.

ary uncertainty. However, the algorithms still work satisfactorily even under the perturbation of uncontrolled boundaries. The errors are summarized in Table 5.4.

6 Concluding remarks

In this paper we have constructed efficient algorithms for imaging point sources and dipoles from limited-view data. Our approach is based on averaging of the limited-view data, using weights constructed by the geometrical control method. It is quite robust with respect to perturbations of the non-accessible part of the boundary. We have shown that if one can

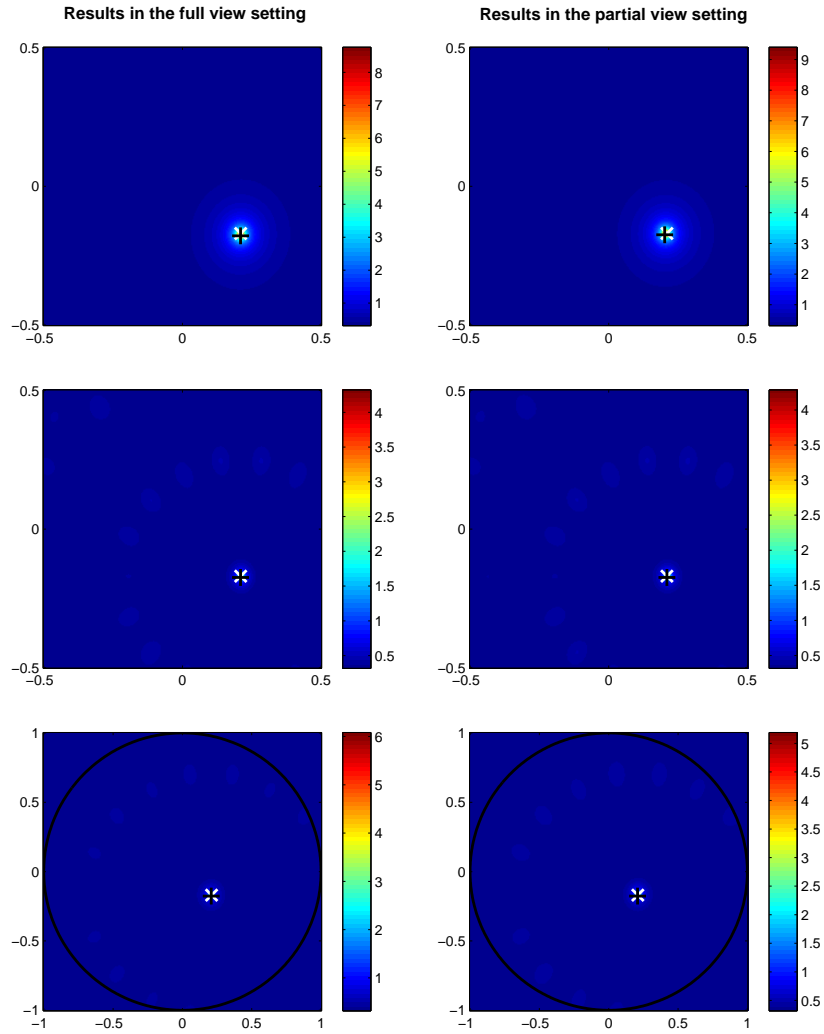


Figure 7: MUSIC results for the geometries of Table 1 - from top to bottom: sqReg0, sqReg2, disc. The (black/white) x denotes the (numerical/theoretical) center of the source.

construct accurately the geometric control then one can perform imaging with the same resolution using partial data as using complete data. The generalization of the proposed algorithms to the case where the speed of sound has random fluctuations will be considered in a forthcoming paper.

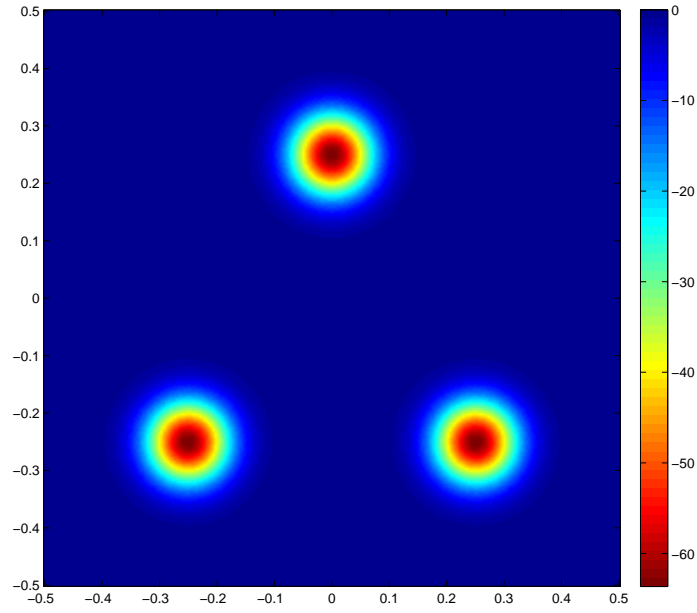


Figure 8: Initial time derivative for the case of multiple sources.

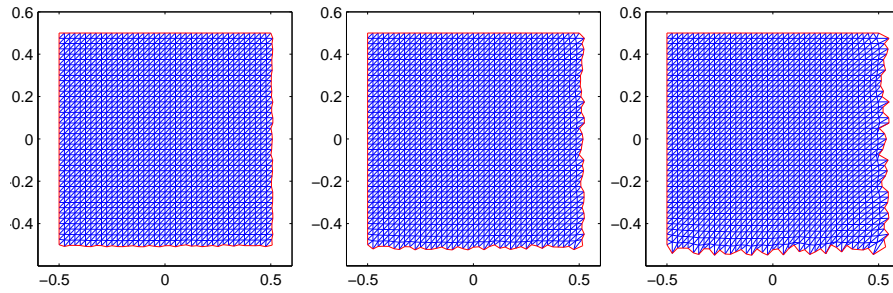


Figure 9: Perturbation of the mesh for $\epsilon = 0.01, 0.025$ and 0.05 .

Acknowledgements

The authors are very grateful to the reviewers for their comments and suggestions to improve the presentation of the paper.

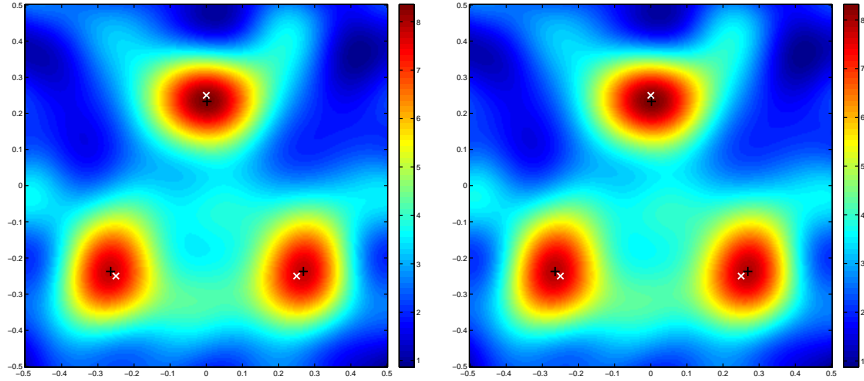


Figure 10: Kirchhoff results for the geometry sqReg2 with several inclusions.

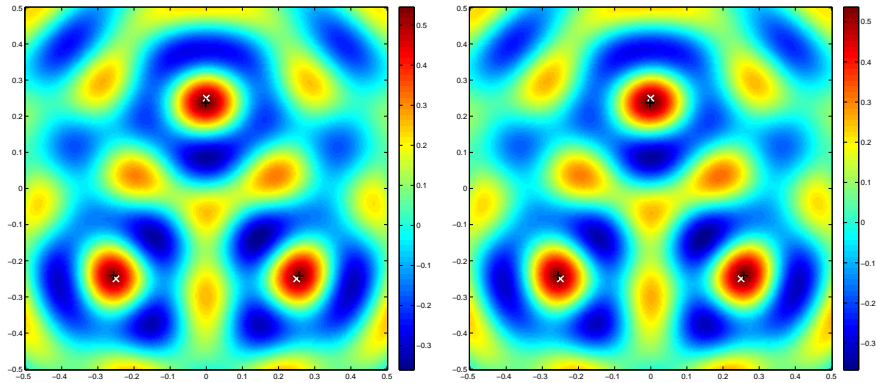


Figure 11: Back-propagation results for the geometry sqReg2 with several inclusions.

References

- [1] H. Ammari, An inverse initial boundary value problem for the wave equation in the presence of imperfections of small volume, *SIAM J. Control Optim.*, 41 (2002), 1194–1211.
- [2] H. Ammari, *An Introduction to Mathematics of Emerging Biomedical Imaging*, Mathematics and Applications, Volume 62, Springer-Verlag, Berlin, 2008.
- [3] H. Ammari, E. Bossy, V. Jugnon, and H. Kang, Mathematical modelling in photoacoustic imaging of small absorbers, *SIAM Rev.*, 52 (2010), 677–695.

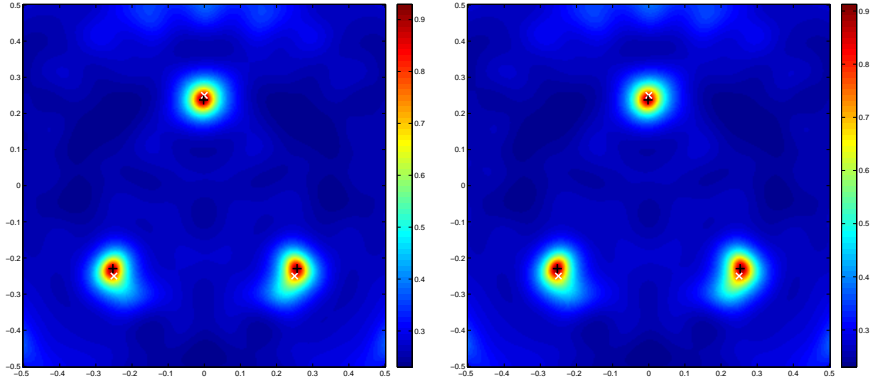


Figure 12: MUSIC results for the geometry sqReg2 with several inclusions.

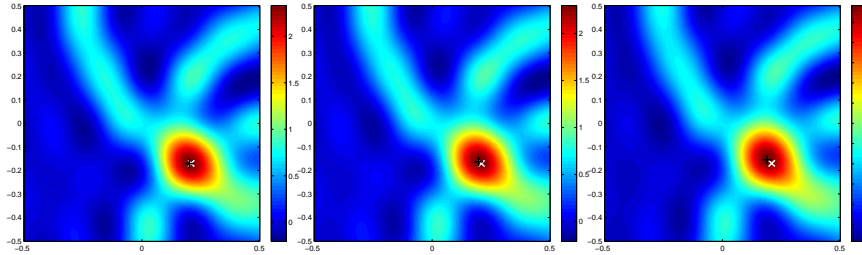


Figure 13: Kirchhoff results for the geometry sqReg2 with perturbed boundary (from left-to-right, $\epsilon = 0.01, 0.025$ and 0.05). The (black/white) x denotes the (numerical/theoretical) center of the source.

- [4] H. Ammari, E. Bretin, V. Jugnon, and A. Wahab, Photoacoustic imaging for attenuating acoustic media, in *Mathematical Modeling in Biomedical Imaging II*, Lecture Notes in Mathematics, Springer-Verlag, Berlin, to appear.
- [5] H. Ammari, Y. Capdeboscq, H. Kang, and A. Kozhemyak, Mathematical models and reconstruction methods in magneto-acoustic imaging, *Euro. J. Appl. Math.*, 20 (2009), 303–317.
- [6] H. Ammari, P. Garapon, L. Guadarrama Bustos, and H. Kang, Transient anomaly imaging by the acoustic radiation force, *J. Diff. Equat.*, 249 (2010), 1579–1595.

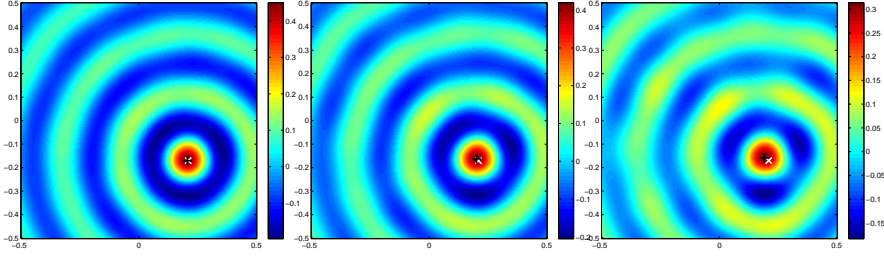


Figure 14: Back-propagation results for the geometry sqReg2 with perturbed boundary (from left-to-right, $\epsilon = 0.01, 0.025$ and 0.05). The (black/white) x denotes the (numerical/theoretical) center of the source.

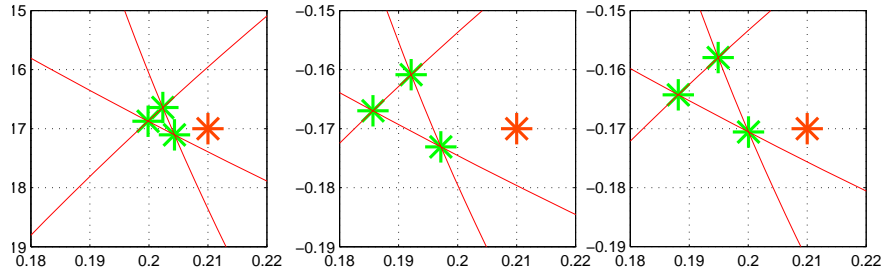


Figure 15: Arrival-time results for the geometry sqReg2 with perturbed boundary (from left-to-right, $\epsilon = 0.01, 0.025$ and 0.05).

- [7] H. Ammari, J. Garnier, V. Jugnon, and H. Kang, Direct reconstruction methods in ultrasound imaging, in *Mathematical Modeling in Biomedical Imaging II*, Lect. Notes in Math., Springer-Verlag, 2011, to appear.
- [8] H. Ammari, J. Garnier, H. Kang, W.K. Park, and K. Sølna, Imaging schemes for perfectly conducting cracks, *SIAM J. App. Math.*, 71 (2011), 68–91.
- [9] H. Ammari, E. Iakovleva, and D. Lesselier, A MUSIC algorithm for locating small inclusions buried in a half-space from the scattering amplitude at a fixed frequency, *SIAM Multiscale Model. Simul.*, 3 (2005), 597–628.

| Algorithm | Perturbation amplitude ϵ | x_{est} | $ x_0 - x_{\text{est}} $ |
|------------------|-----------------------------------|------------------|--------------------------|
| Kirchhoff | 0.01 | [0.2020 -0.1706] | 0.0081 |
| | 0.025 | [0.1980 -0.1628] | 0.0140 |
| | 0.05 | [0.1902 -0.1549] | 0.0249 |
| Back-propagation | 0.01 | [0.2058 -0.1706] | 0.0042 |
| | 0.025 | [0.2020 -0.1628] | 0.0108 |
| | 0.05 | [0.1902-0.1588] | 0.0227 |
| Arrival time | 0.01 | [0.2022 -0.1687] | 0.0079 |
| | 0.025 | [0.1917 -0.167] | 0.0186 |
| | 0.05 | [0.1944 -0.1643] | 0.0166 |

Table 3: Numerical results for localization of the source at $x_0 = [0.21 \ -0.17]$ using sqReg2 geometry with boundary perturbations.

- [10] H. Ammari, E. Iakovleva, D. Lesselier, and G. Perrusson, A MUSIC-type electromagnetic imaging of a collection of small three-dimensional inclusions, *SIAM J. Sci. Comput.*, 29 (2007), 674–709.
- [11] H. Ammari and H. Kang, Reconstruction of elastic inclusions of small volume via dynamic measurements, *Appl. Math. Opt.*, 54 (2006), 223–235.
- [12] H. Ammari and H. Kang, *Expansion Methods*, Chap. 9 in *Handbook of Mathematical Methods in Imaging*, Springer-Verlag, New York, 2011.
- [13] M. Asch and G. Lebeau, Geometrical aspects of exact boundary controllability for the wave equation—a numerical study, *ESAIM Control Optim. Calc. Var.*, 3 (1998), 163–212.
- [14] C. Bardos, A mathematical and deterministic analysis of the time-reversal mirror, in *Inside Out: Inverse Problems*, MSRI Publications, Vol. 47, 2003.
- [15] C. Bardos, G. Lebeau, and J. Rauch, Sharp sufficient conditions for the observation, control, and stabilization of waves from the boundary, *SIAM J. Control Optim.*, 30 (1992), 1024–1065.
- [16] M. I. Belishev, Recent progress in the boundary control method, *Inverse Problems*, 23 (2007), R1–R67.
- [17] J. Benesty, J. Chen, and Y. Huang, Time-delay estimation via linear interpolation and cross correlation, *IEEE Trans. Speech Audio Process.*, 12 (2004), 509–519.
- [18] J. Bercoff, M. Tanter, and M. Fink, Supersonic shear imaging: a new technique for soft tissue elasticity mapping, *IEEE Trans. Ultrasonics, Ferro., Freq. Control*, 51 (2004), 396–409.
- [19] J. Bercoff, M. Tanter, M. Muller, and M. Fink, The role of viscosity in the impulse diffraction field of elastic waves induced by the acoustic radiation force, *IEEE Trans. Ultrasonics, Ferro., Freq. Control*, 51 (2004), 1523–1536.
- [20] A. C. Birch and A. G. Kosovichev, Travel time sensitivity kernels, *Solar Phys.*, 192 (2000), 193–201.

- [21] G. C. Carter, Special Issue on Time-Delay Estimation, *IEEE Trans. Acoust., Speech, Sig. Process.*, vol. ASSP-29, June 1981.
- [22] Y. T. Chan and K. C. Ho, A simple and efficient estimator for hyperbolic location, *IEEE Trans. Sig. Process.*, 42 (1994), 1905–1915.
- [23] J. C. Chen, K. Yao, and R. E. Hudson, Source localization and beamforming, *IEEE Sig. Process. Magazine*, March 2002, 30–39.
- [24] M. Cheney, The linear sampling method and the MUSIC algorithm, *Inverse Problems*, 17 (2001), 591–595.
- [25] B. T. Cox, S. R. Arridge, and P. C. Beard, Photoacoustic tomography with a limited-aperture planar sensor and a reverberant cavity, *Inverse Problems* 23 (2007), S95–S112.
- [26] A. J. Devaney, Time reversal imaging of obscured targets from multistatic data, *IEEE Trans. Antennas Propagat.*, 523 (2005), 1600–1610.
- [27] P. Docherty, A brief comparison of some Kirchhoff integral formulas for migration and inversion, *Geophysics*, 56 (1991), 1164–1169.
- [28] M. Fink, Time reversed acoustics, *Physics Today* 50 (1997), 34.
- [29] M. Fink, Time-reversal acoustics in *Inverse Problems, Multi-Scale Analysis and Homogenization*, 151–179, edited by H. Ammari and H. Kang, *Contemp. Math.*, Vol. 408, Rhode Island, Providence, 2006.
- [30] A. R. Fisher, A. J. Schissler, and J. C. Schotland, Photoacoustic effect of multiply scattered light, *Phys. Rev. E*, 76 (2007), 036604.
- [31] R. Glowinski, Ensuring well posedness by analogy; Stokes problem and boundary control for the wave equation, *J. Comput. Phys.*, 103 (1992), 189–221.
- [32] R. Glowinski and C. H. Li, On the numerical implementation of the Hilbert uniqueness method for the exact boundary controllability of the wave equation, *C. R. Acad. Sci. Paris Sér. I Math.*, 311 (1990), 135–142.
- [33] R. Glowinski, C. H. Li, and J. L. Lions, A numerical approach to the exact boundary controllability of the wave equation. I. Dirichlet controls: description of the numerical methods, *Japan J. Appl. Math.*, 7 (1990), 1–76.
- [34] G. Lebeau, Control of hyperbolic equations, *Journées Equat. Dérivées Part.*, 1992, 1–24.
- [35] S. Hou, K. Sølna, and H. Zhao, A direct imaging method using far field data, *Inverse Problems*, 23 (2007), 1533–1546.
- [36] Y. Huang, J. Benesty, G. W. Elko, and R. M. Mersereau, Real-time passive source localization: a practical linear-correction least-squares approach, *IEEE Trans. Speech Audio Process.*, 9 (2001), 943–956.
- [37] L. I. Ignat and E. Zuazua, Convergence of a two-grid algorithm for the control of the wave equation, *J. Europ. Math. Soc.*, 11 (2009), 351–391.

- [38] M. R. Islam and B. C. Towe, Bioelectric current image reconstruction from magneto-acoustic measurements, *IEEE Trans. Med. Img.* 7 (1988), 386–391.
- [39] A. G. Kosovichev, T. L. Duvall, and P. H. Scherrer, Time-distance inversion methods and results, *Solar Phys.*, 192 (2000), 159–176.
- [40] L. A. Kunyansky, Thermoacoustic tomography with detectors on an open curve: an efficient reconstruction algorithm, *Inverse Problems* 24 (2008), 055021.
- [41] J. L. Lions, *Contrôlabilité exacte, Perturbations et Stabilisation de Systèmes Distribués*, Tome 1, Contrôlabilité exacte, Masson, Paris, 1988.
- [42] G. Paltauf, R. Nuster, M. Haltmeier, and P. Burgholzer, Experimental evaluation of reconstruction algorithms for limited view photoacoustic tomography with line detectors, *Inverse Problems* 23 (2007), S81–S94.
- [43] S. K. Patch, Thermoacoustic tomography–consistency conditions and the partial scan problem, *Phys. Med. Biol.*, 49 (2004), 1–11.
- [44] B. J. Roth and P. J. Basser, A model of the stimulation of a nerve fiber by electromagnetic induction, *IEEE Trans. Biomed. Eng.*, 37 (1990), 588–597.
- [45] B. J. Roth, P. J. Basser, and J. P. Jr Wikswo, A theoretical model for magneto-acoustic imaging of bioelectric currents, *IEEE Trans. Biomed. Eng.*, 41 (1994), 723–728.
- [46] H. C. Schau and A. Z. Robinson, Passive source localization employing intersecting spherical surfaces from time-of-arrival differences, *IEEE Trans. Acoust. Speech, Process.*, 35 (1987), 1223–1225.
- [47] M. Wax and T. Kailath, Optimum localization of multiple sources by passive arrays, *IEEE Trans. Acoust. Speech, Process.*, 31 (1983), 1210–1217.
- [48] M. Xu and L. V. Wang, Photoacoustic imaging in biomedicine, *Review of Scientific Instruments* 77 (2006), 041101.
- [49] E. Zuazua, Propagation, observation, and control of waves approximated by finite difference methods, *SIAM Rev.*, 47 (2005), 197–243.